ACCSCIENCE PUBLISHING

International Journal of Bioprinting

RESEARCH ARTICLE

A scalable 3D-printed brain tumour model for high-throughput screening glioblastoma biology and drug response

Panthipa Suwannakot[1,2], Eva Tomaskovic-Crook[1,2,3]*, Kimberley L. Alexander[2,4,5], and Jeremy Micah Crook[1,2,3]*

[1]Arto Hardy Family Biomedical Innovation Hub, Chris O'Brien Lifehouse, Sydney, NSW 2050, Australia

[2]School of Medical Sciences, Faculty of Medicine and Health, The University of Sydney, NSW 2006, Australia

[3]Intelligent Polymer Research Institute, Australian Institute of Innovative Materials, Innovation Campus, University of Wollongong, NSW 2500, Australia

[4]Brain Cancer Research, Chris O'Brien Lifehouse, Sydney, NSW 2050, Australia

[5]Department of Neuropathology, Royal Prince Alfred Hospital, Sydney, NSW 2050, Australia

Abstract

Glioblastoma (GBM) is a highly aggressive brain tumour characterised by its rapid infiltrative growth patterns, marked intra- and inter-tumoural heterogeneity, and resistance to conventional treatments. GBM has a median overall survival of 15 months and a 5-year survival rate of approximately 5%. Current treatment modalities, including surgery and chemoradiotherapy, have shown limited success. To address the need for more effective therapeutic strategies and a deeper understanding of GBM biology, we utilised droplet printing technology to fabricate a high-throughput 3D brain tumour model. We first optimised the printability of the GBM cell-laden gelatin methacrylate (GelMA) bioink, tailoring its mechanical properties to mimic the stiffness of human brain tissue. Next, we employed metabolic and immunofluorescence assays to investigate the response of the printed GBM droplets to the standard-of-care chemotherapeutic agent temozolomide (TMZ). Furthermore, using droplet digital PCR (ddPCR), we assessed the expression of microRNAs typical for paediatric GBM (miR-490, miR-876-3p, miR-876-5p, miR-448, miR-137, and miR-501-3p), with miR-191-5p used as the endogenous control. Our approach provides proof-of-concept for high-throughput screening of GBM drug response. Moreover, our 3D-printed brain tumour model could be used for patient-personalised tumour screening, encompassing theranostics for GBM diagnostics, treatment, and monitoring.

Keywords: Glioblastoma; Drug resistance; Drug screening; 3D bioprinting; Gelatin methacrylate; Hydrogel; MicroRNA

***Corresponding authors:**
Eva Tomaskovic-Crook (eva.tomaskoviccrook@lh.org.au); Jeremy Micah Crook (jeremy.crook@lh.org.au)

Citation: Suwannakot P, Tomaskovic-Crook E, Alexander KL, Crook JM. A scalable 3D-printed brain tumour model for high-throughput screening glioblastoma biology and drug response. *Int J Bioprint.* 2026;12(5):026330357. doi: 10.36922/IJB026330357

Received: December 19, 2025

Revised: August 13, 2026

Accepted: August 26, 2026

Published online: August 26, 2026

Copyright: © 2026 Author(s). This is an Open-Access article distributed under the terms of the Creative Commons Attribution License, permitting distribution, and reproduction in any medium, provided the original work is properly cited.

Publisher's Note: AccScience Publishing remains neutral with regard to jurisdictional claims in published maps and institutional affiliations.

1. Introduction

Glioblastoma (GBM) is a highly aggressive and invasive brain tumour.[1] It grows rapidly and resists traditional treatments. GBM was previously thought to arise from differentiated glial cells. However, genomic and lineage-tracing studies now support a shift toward a

molecularly defined framework in which GBM may arise from multiple precursor populations, including neural stem and progenitor cells of the subventricular zone[2,3] The average survival time after initial diagnosis is only 15 months, with a 5-year survival rate of approximately 5%.[4,5]

The standard first-line treatment for GBM involves maximal safe surgical resection, followed by radiotherapy with concomitant and adjuvant temozolomide (TMZ) chemotherapy. Despite this intensive multimodal approach, GBM remains challenging to treat due to its highly infiltrative growth, marked tumoural heterogeneity, therapeutic resistance, and inevitable recurrence. Consequently, there is a pressing need for more effective treatment strategies and advanced research tools to better understand GBM biology and enable the development of improved therapies. Notably, despite promising results in conventional preclinical testing, many experimental GBM therapies have failed in clinical trials.[6] This disconnect highlights the limitations of existing preclinical models and underscores the need for more clinically relevant experimental systems that better capture the inherent complexity of primary GBM. Improved models are vital for identifying risk factors, understanding treatment resistance, and evaluating novel therapies.

Until recently, planar (two-dimensional; 2D) cell culture and *in vivo* mouse models have been the mainstay for preclinical GBM research. However, 2D cell cultures fail to recapitulate the complex three-dimensional (3D) tumour tissue architecture, including the tumour microenvironment with critical cell-cell and cell-matrix interactions. Similarly, animal models do not faithfully replicate human physiology or the molecular and behavioural characteristics of human GBM. Collectively, these limitations underscore the need for more human-like GBM tissue models that incorporate genetically relevant human cells and are scalable for the systematic investigation of tumour progression and therapeutic response in a physiologically relevant environment. 3D spheroid and organoid technologies are examples of emerging pre-clinical avatars for such precision oncology, permitting more physiologically relevant drug screening than conventional 2D cultures.[7,8]

3D bioprinting offers further possibilities for improved preclinical GBM modelling, including more patient-personalised pharmacotherapy. This approach utilises printed bioinks comprising cell-laden biomaterials or acellular biomaterials, with the latter seeded with cells post-printing. Hydrogels are attractive for GBM and other cancer tissue bioprinting due to their high tissue-mimicking water content and tunable biochemical and physical properties.[9,10] Gelatin methacrylate (GelMA) is an inexpensive hydrogel, used by our group and others for engineering and modelling human neural tissue[11,12] and GBM biology.[13] GelMA is a versatile, reliable and bioactive semisynthetic matrix derived from collagen, and comprises natural cell-binding motifs, including RGD (arginine-glycine-aspartic acid; the principal integrin-binding domain within the extracellular matrix), matrix metalloproteinase-sensitive degradation sites for proteolytic breakdown and cell migration, as well as various amino acid side chain functionalities for covalent modification. Importantly, GelMA remains stable at 37 °C, which is vital for tissue engineering.

MicroRNA (miRNA) profiles derived from bioprinted GBM models have significant potential as diagnostic and prognostic indicators. miRNAs are short (19–24 nucleotides), single-stranded, non-coding RNAs that regulate gene expression at the post-transcriptional level by promoting mRNA degradation or inhibiting translation, thereby reducing protein expression.[14] Through these mechanisms, miRNAs play essential roles in cell growth, proliferation, differentiation, viability, and apoptosis, and are involved in embryonic development, cellular signalling, and pathological processes, including cancer.[15-19] The dysregulation of miRNAs in GBM supports their utility as diagnostic markers and potential targets for GBM treatment.[20,21] For example, miR-21 is consistently overexpressed in glioma tumours and cell lines, with expression levels correlating with tumour grade and disease progression.[22,23] Furthermore, miRNAs have been implicated in regulating TMZ resistance in GBM through drug metabolism, absorption, DNA repair, and cell cycle regulation.[24,25] Specific miRNAs are expressed in paediatric GBM, including miR-490, miR-137-5p, miR-876-3p, miR-876-5p, miR-448, and miR-501-3p (Table S1), which are potentially relevant to chemoresistance in high-grade glioma.[14]

Here, we describe a well-defined and reproducible method for high-throughput bioprinting 3D human micro-tumour constructs (tumouroids) using an optimally tuned GelMA hydrogel-based bioink for preclinical modelling of GBM. More specifically, the tumouroids model paediatric high-grade gliomas (pHGGs) and were generated using well-established SF188 and KNS42 cell lines. We have demonstrated the utility of tumouroids for molecular (including miR) and phenotypic characterisation in chemotherapeutic drug screening. We initially optimised the rheological properties of GelMA for GBM cell encapsulation and printing, ensuring suitable GBM-ink viscosity before and during printing, followed by gelation by photo-crosslinking (Figure 1a). The stiffness/modulus of gelated GelMA was tailored to

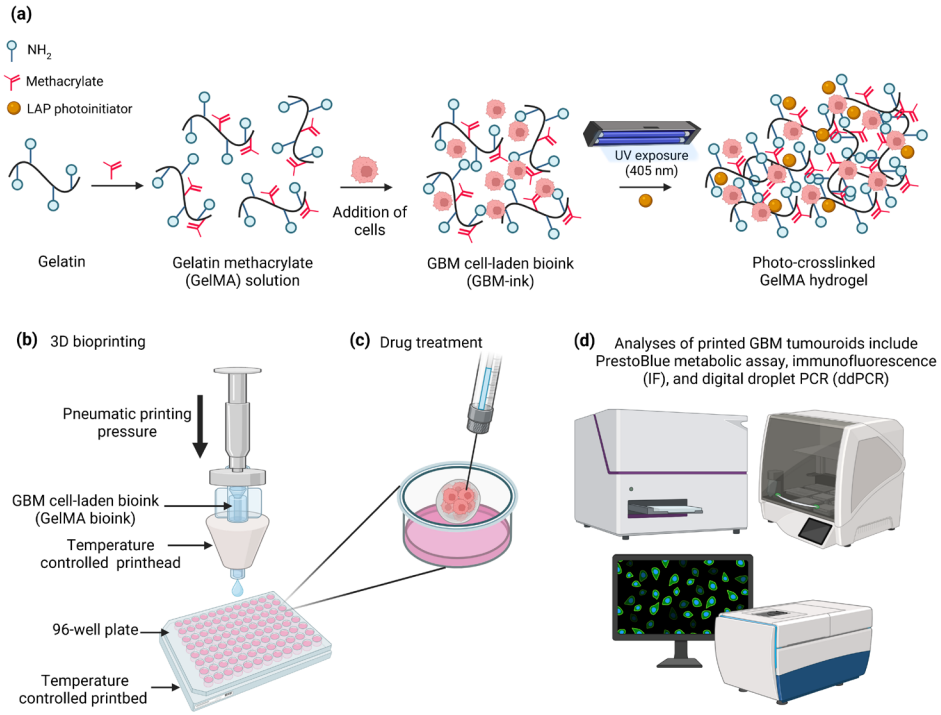


Figure 1. Schematic illustrating the major components and/or stages of bioprinting 3D human micro-tumour constructs (tumouroids) using an optimally tuned GelMA hydrogel-based bioink for preclinical modelling of GBM. (a) Synthesis of cell-laden GelMA hydrogel by reacting gelatin with methacrylate, subsequent addition of GBM cells to form the cell-laden bioink (GBM-ink), and gelation by crosslinking with UV photoinitiator (lithium phenyl-2,4,6-trimethylbenzoylphosphinate, LAP). (b) High-throughput droplet-based printing of GBM-ink. (c) Drug treatment. (d) Molecular and phenotypic analyses of printed GBM tumouroids.

mimic native human brain tissue, providing a supportive niche for GBM cell survival. Importantly, tumouroids were printed into 96-well plates (Figure 1b) to rapidly generate uniform arrays for scalable drug treatment (Figure 1c) and subsequent analyses, including comparisons of clinically relevant miRNA expression and expression of the DNA repair enzyme O^6-methylguanine-DNA methyltransferase (MGMT) between cell-line specific tumouroids. We selected six miRNAs (miR-490, miR-137 5p, miR-876 3p, miR-876 5p, miR-448, miR-501 3p) because they are reported to be dysregulated in paediatric GBM.[14] Other independent publications have subsequently linked each of these miRNAs to tumour-suppressive functions or to chemoresistance mechanisms (including TMZ resistance). We therefore aimed to explore how TMZ treatment modulates the expression of the miRNAs that are already known to be relevant to drug response pathways in paediatric GBM.

Our approach provides proof of concept for the high-throughput production of human GBM tumour tissues *in vitro*, enabling the study of tumour biology and treatment response. Our 3D-printed brain tumour model could be used for patient-personalised tumour screening and may support theranostic applications in GBM diagnosis, treatment and monitoring.

2. Materials and methods

2.1. Preparation of GelMA solutions

Freeze-dried ethylene oxide-sterilised GelMA (37% degree of functionalisation [DoF], 300 bloom, porcine skin; The Australian National Fabrication Facility (ANFF) Materials Node, University of Wollongong, Australia) was stored at −80°C protected from light. GelMA stock solution (10.0% w/v) was prepared by dissolving GelMA (1.0 g) in pre-warmed (37 °C) Dulbecco's phosphate-buffered saline (DPBS; 10 mL; Gibco, ThermoFisher Scientific) with gentle vortexing, followed by incubation in a 37 °C water bath for approximately 30 min. The solution was stored protected from light at 4 °C until further use. A 2.5% (w/v) stock solution of lithium phenyl-2,4,6-trimethylbenzoylphosphinate (LAP) was prepared by dissolving LAP (0.25 g) in DPBS (10 mL), under light-protected conditions. The solution was sterilised using a 0.22 µm filter and stored at 4 °C until further use. Working

GelMA formulations (2.5%–7.5% w/v) were prepared by mixing pre-warmed GelMA stock solution with LAP stock solution and DPBS to achieve the desired final GelMA concentration and a final LAP concentration of 0.25% (w/v). For example, to prepare 1 mL of a 5% (w/v) GelMA solution containing 0.25% (w/v) LAP, 0.5 mL of 10% (w/v) GelMA stock, 0.1 mL of 2.5% (w/v) LAP stock and 0.4 mL of DPBS were combined.

2.2. Planar/2D cell culture

SF188 paediatric human GBM cells (Merck, Darmstadt, Germany) were cultured in low-glucose (1.0 g/L D-glucose) Dulbecco's Modified Eagle Medium (DMEM; Gibco, ThermoFisher Scientific, Australia), supplemented with 10% (v/v) fetal bovine serum (FBS) and 1× GlutaMAX™ Supplement (Gibco, Thermo Fisher Scientific). KNS42 paediatric human GBM cells (CellBank Australia, Children's Medical Research Institute, Sydney, Australia) were cultured in DMEM F-12 (Thermo Fisher Scientific), supplemented with 5% (v/v) FBS and 1 × GlutaMAX™ Supplement. Both cell lines were maintained in T75 tissue culture flasks at 37 °C in a humidified atmosphere with 5% CO_2. Cell culture medium was refreshed every 3–4 days and cells were passaged at 80%–90% confluence. Passaging involved a DPBS wash followed by incubation with 0.25% (w/v) Trypsin-EDTA (Gibco, Thermo Fisher Scientific) for 3–4 min. Trypsin activity was neutralised by the addition of an equal volume of complete culture medium, and cells were collected by centrifugation at 300× *g* for 5 min. Cells were counted using a Countess 3 automated cell counter (Thermo Fisher Scientific) and re-seeded for further culture.

2.3. Rheology

Rheological measurements were performed using a Kinexus Prime Ultra$^+$ rotational rheometer (NETZSCH Australia Pty Ltd, Sydney, Australia). Temperature-dependent viscosity of GelMA was measured over a range of 10–40 °C using cone-plate geometry (CP1/50 L2540 SS). GelMA samples (580 µL) were loaded between the cone and plate with a fixed gap height of 0.1504 mm. Viscosity (Pa·s) was measured as a function of shear rate using a stepwise shear-rate ramp from 1000 s^{-1} to 0.01 s^{-1} with 10 measurement points per decade. All measurements were performed in duplicate. Rheological data were processed using rSpace software (NETZSCH) and plotted using GraphPad Prism version 9.3.1 (GraphPad Software Inc., La Jolla, California).

The viscoelastic properties of GelMA hydrogels were assessed using the same rheometer equipped with a parallel plate geometry (20 mm diameter, PU20 L1926 SS). GelMA samples (357 µL) were prepared at the desired concentrations and cast into wells of a 24-well plate (Corning, Costar, Merck, Darmstadt, Germany) to achieve a depth of approximately 1.4 mm. Samples were polymerised using UV light (52.4 mW/cm^2 for 120 s), followed by incubation in DMEM (1 mL) for 30 min at either 25 °C or 37 °C prior to measurements. Oscillatory rheological measurements were performed with a fixed gap height of 1 mm. Strain amplitude sweep tests were conducted to determine the linear viscoelastic region, followed by frequency-sweep measurements at a fixed strain amplitude of 0.1% and an angular frequency range centred at 1 Hz. Storage (G') and loss (G") moduli were recorded as functions of strain amplitude and frequency at both 25 °C and 37 °C.

2.4. Bioink preparation and 3D bioprinting

3D bioprinting was performed using a BIO X6 bioprinter equipped with a temperature-controlled printhead (CELLINK, Gothenburg, Sweden). Prior to printing, the printing chamber was sterilised with 70% ethanol followed by a 10 min UV sterilisation cycle. The printhead and printbed were equilibrated to 25 °C and 10 °C, respectively. Bioink was prepared by resuspending cell pellets in pre-warmed 5% (w/v) GelMA/LAP in DPBS at a density of 6×10^6 cells/mL. The bioink was transferred into a 3 mL printing cartridge (Nordson EFD) fitted with an end cap and tip cap. The tip cap was replaced with a 22-gauge tapered nozzle (22G, 410 µm inner diameter, Nordson EFD) and the end cap was replaced with a cartridge adapter. The loaded cartridge was inserted into the temperature-controlled printhead (CELLINK). Bioink was extruded into individual wells of 96-well plates (Corning, Costar, Merck, Darmstadt, Germany) using a droplet-based printing mode and standard G-code generated in the printer software. Printability and droplet size were optimised by adjusting print bed and printhead temperatures, extrusion pressure and time, and UV crosslinking duration. Following printing, culture medium (200 µL) was added to each well and the printed constructs were incubated at 37 °C in a humidified atmosphere containing 5% CO_2.

2.5. Temozolomide treatment of 3D-bioprinted tumouroids

TMZ solid (5 mg) was dissolved in Milli-Q water to obtain a stock concentration of 10 mM. Serial dilutions were prepared in low-glucose (1.0 g/L D-glucose) DMEM supplemented with 10% (v/v) FBS and 1 × GlutaMAX™ Supplement to obtain a concentration range of 1000, 500, 250, 125, 62.5, 31.25 and 15.6 µM. Bioprinted tumouroids were cultured for 2 days prior to treatment, after which culture medium was removed and replaced with 100 µL of TMZ-containing medium at the indicated concentrations. Control tumouroids received vehicle-only

culture medium. Samples were incubated at 37 °C in a humidified atmosphere containing 5% CO_2 for 4 days. A 2-day pretreatment interval was chosen to: (i) allow cell recovery from extrusion printing, (ii) permit initial matrix remodelling to stabilise the construct, (iii) ensure high cell viability of cultured tumour constructs, and (iv) enable timely drug screening.

2.6. Metabolic activity assay

Metabolic activity of printed tumouroids following TMZ treatment was assessed using PrestoBlue™ Cell Viability Assay (Thermo Fisher Scientific). PrestoBlue reagent (10% v/v) was added to each well of a 96-well plate, and the plate was incubated for 1.5 h at 37 °C. Fluorescence from triplicate technical replicates of the supernatant was measured using a CLARIOstar plate reader (BMG LabTECH, Germany) with excitation at 544 nm and emission at 590 nm.

2.7. Immunohistochemistry and analysis

Spatial mapping of MGMT protein expression was enabled by fluorescence immunohistochemistry. Tumouroids were washed twice in PBS at room temperature for 5 min each, fixed in 4% paraformaldehyde (PFA) at room temperature for 30 min, and washed twice in PBS for 5 min each. Samples were then permeabilised with 0.3% (v/v) Triton X-100 in PBS for 30 min at room temperature and blocked with 5% (v/v) donkey serum (Sigma-Aldrich, USA) overnight at 4 °C. Constructs were labelled with primary anti-MGMT antibody (1:200, Sigma, USA) diluted in 5% (v/v) donkey serum in PBS overnight at 4 °C, followed by incubation with a species-specific Alexa Fluor 488-conjugated secondary antibody (anti-rabbit IgG (H+L); 1:1000, Thermo Fisher Scientific) in 5% (v/v) donkey serum in PBS overnight at 4 °C. Tumouroids were washed four times in 0.1% Triton X-100 in PBS for 10 min per wash, and counterstained with DAPI (1:1000, Thermo Fisher Scientific) in PBS for 10 min at room temperature. The constructs were imaged using a Leica Thunder Imaging System (Leica Microsystems, Wetzlar, Germany). Images were processed with LAX S software (Leica Microsystems) and analysed using Fiji (Image J).[26] Integrated Density (IntDen; product of mean grey value and area) was measured for three randomly selected regions of interest (ROIs) per construct and corrected for background signal.[27,28] MGMT expression was normalised to nuclear area by calculating MGMT IntDen per total DAPI-positive area. Data were fitted using a four-parameter logistic (4-PL) model in GraphPad Prism version 9.3.1 (GraphPad Software Inc., La Jolla, California).

2.8. RNA extraction

Tumouroids were cultured for 48 h and treated with TMZ for 4 days (96 h). Following the treatment, tumouroids were washed five times with DPBS at room temperature, at 5 min intervals, to remove residual TMZ, and were then stored at −80 °C for subsequent RNA extraction. Total RNA was extracted using TRIzol® (300 µL) according to the manufacturer's instructions. RNA concentration and purity were assessed spectrophotometrically using a CLARIOstar plate reader (BMG LabTECH, Germany). Extracted RNA was stored short-term at −20 °C. RNA integrity was evaluated using an Agilent 4200 TapeStation with the RNA ScreenTape assay, and only samples with an RNA integrity number (RIN) ≥ 7.5 were included in the droplet digital polymerase chain reaction (ddPCR) analysis.

2.9. cDNA synthesis

Approximately 5 ng of total RNA was reverse transcribed and pre-amplified using the TaqMan® Advanced miRNA cDNA Synthesis Kit (Thermo Fisher Scientific, A25576), according to the manufacturer's protocol on a C1000 Touch™ thermal cycler (Bio-Rad, #CT063465). Briefly, total RNA was subjected to poly(A) tailing at 37 °C for 45 min, followed by enzyme inactivation at 65 °C for 10 min and a hold at 4 °C.

Adaptor ligation was then performed at 16 °C for 60 min, followed by a hold at 4 °C. Reverse transcription was carried out at 42 °C for 15 min, followed by enzyme inactivation at 85 °C for 5 min, and a hold at 4 °C. The resulting cDNA was pre-amplified using the miR-Amp reaction with an initial enzyme activation step at 95 °C followed by 14 cycles of denaturation at 95 °C for 3 s and annealing/extension at 60 °C for 30 s, and a final stop reaction at 99 °C for 10 min. miR-Amp reaction products were aliquoted and stored at −20 °C until downstream ddPCR analysis.

2.10. Droplet digital PCR

A QX 200 ddPCR system (Bio-Rad, Solna, Sweden) was used according to the manufacturer's instructions unless stated otherwise. The following miRNA targets were assayed: hsa-miR-490-5p (Assay ID: 478941_mir, Thermo Fisher), hsa-miR-137-5p (Assay ID: 483102_mir, Thermo Fisher), hsa-miR-876-3p (Assay ID: 479186_mir, Thermo Fisher), hsa-miR-876-5p (Assay ID: 479187_mir, Thermo Fisher), hsa-miR-448 (Assay ID: 478105_mir, Thermo Fisher), and hsa-miR-501-3p (Assay ID: 478350_mir, Thermo Fisher), hsa-miR-191-5p (Assay ID: 477952_mir, Thermo Fisher) was used as the endogenous control. The expression of the target miRNA was normalised relative to hsa-miR-191-5p expression (Table S1). Although miR-191-5p has been reported to have oncogenic activity in some cancer types, its high stability under our experimental conditions

supports its use as a reliable normaliser that does not bias the comparative expression results presented.

Probe fluorophores were FAM. Briefly, a 22 µL PCR reaction consisted of 11 µL of 1× ddPCR Supermix with no dTUP, primers (900 nM), probes (250 nM), 1.1 µL TaqMan miRNA Assay (Thermo Fisher), 4.4 µL RNase- and DNase-free water and 5.5 µL of 10 times dilution cDNA. Subsequently, the droplets were generated with 70 µL of Bio-Rad Droplet Generation Oil (Bio-Rad) and 20 µL PCR mix using an automated QX 200 droplet generator (Bio-Rad, Solna, Sweden). Next, a total volume of 90 µL of generated droplets from each well was transferred automatically to a ddPCR™ 96-well plate (Bio-Rad, Solna, Sweden). The plate was heat-sealed with pierceable foil at 180°C using the PX1™ Plate Sealer (Bio-Rad).

PCR amplification was performed using a C1000 Touch™ thermal cycler (Bio-Rad, #CT063465). Cycling conditions consisted of an initial denaturation step at 95 °C for 10 min, followed by 40 cycles of denaturation at 94 °C for 30 s and annealing at 59 °C for 60 s and a final enzyme deactivation step at 98 °C for 10 min, with a hold at 4 °C. In all steps, the ramping rate was set to 2 °C/s. Following amplification, the plates were transferred to a QX200 droplet reader (Bio-Rad), for absolute quantification via laser-based detection of fluorescently labelled amplicons within individual droplets. Data were analysed using QuantaSoft analysis software (Bio-Rad, version 1.4.0.99). Only samples containing >20,000 droplets were included in downstream analyses. All miRNA quantification experiments included no-template control (NTC) and buffer control wells.

2.11. Statistical analysis

GraphPad Prism version 9.3.1 software (GraphPad Software Inc., La Jolla, California) was used for graphing and statistical analyses. Data are represented as mean ± standard deviation (SD) from at least two independent experiments. Statistical differences were determined by a two-way analysis of variance (ANOVA) with a Bonferroni post hoc test for multiple comparisons. Statistical assumptions were evaluated by testing data normality using the Shapiro–Wilk test and homogeneity of variance using the Brown–Forsythe test. Homogeneity of variance was satisfied ($p > 0.05$), with statistical significance of two-way ANOVA set at $p < 0.05$. No statistical methods were used to predetermine sample sizes; experiments were replicated to reduce variability and minimise errors in statistical testing. Data collection and analysis were performed without blinding to experimental conditions, and samples were not randomised.

3. Results and discussion

3.1. Rheology of GelMA

3.1.1. Viscosity and printability of GelMA solution

Since GelMA is thermoreversible (Figure 2a),[29] a temperature sweep (ranging from 5 °C to 40 °C) was conducted to determine the conditions for optimal viscosity and printing. GelMA solution became more viscous with decreasing temperature, regardless of concentration, while remaining printable within a temperature range of 25 °C to 40 °C (Figure 2b). Below 25 °C, the viscosity was too high to extrude, consistent with GelMA undergoing a sol-gel transition at lower temperatures.[30,31] Consequently, we printed GelMA at room temperature to avoid excessively low or high viscosity. At 25 °C, the viscosities of 2.5%, 5.0%, and 7.5% (w/v) GelMA solutions were 0.012 ± 0.002, 0.345 ± 0.02, and 142.8 ± 3.4 Pa·s, respectively. Additionally, shear-thinning behaviour was observed for all GelMA concentrations, in which the viscosity decreased with increasing shear rate and shear-thinning was more pronounced at higher concentrations of GelMA (Figure 2c).

The optimum printing parameters for GelMA are summarised in Table 1. Specifically, a printbed temperature of 10 °C ensured thermal gelation of the printed GelMA, thereby maintaining droplet shape fidelity before UV crosslinking. The printhead temperature was maintained between 24 °C and 26 °C and the printing pressure was 16–20 kPa for a droplet volume of ~6–8 µL. Finally, the duration of UV crosslinking was fixed at 45 s (Figure 2d).

Table 1. Optimised parameters for printing GelMA (5% w/v with 0.25% LAP) hydrogel droplets using the CELLINK BIO X6 bioprinter

Printing setting	Requirement
Printing pressure (kPa)	16–20
Extrusion time (s)	0.4–0.8
Nozzle diameter (µm)	22 (inner diameter = 410)
Printhead temperature (°C)	24–26
Print bed temperature (°C)	10
UV crosslinking time (s)	45

3.1.2. Stiffness of GelMA hydrogel

To mimic the stiffness of tumour tissue, we first examined the storage modulus of GelMA hydrogels at varying concentrations (2.5%, 5.0%, 7.5% and 10.0% w/v) and temperatures (25 °C and 37 °C) (Figure 3a). As expected,

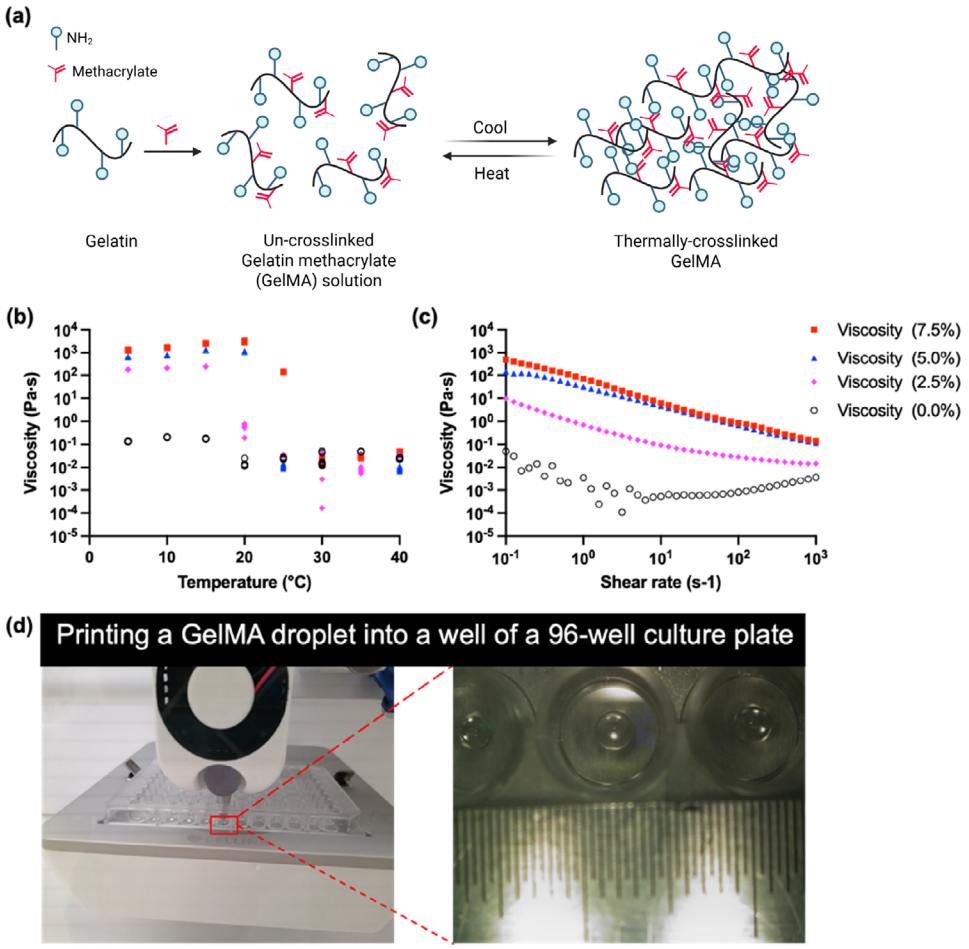


Figure 2. Effect of temperature and shear rate on GelMA viscosity and printability. (a) A schematic of the thermoreversible sol-gel state of GelMA solution. The printability of GelMA solution was optimised by assessing viscosity as a function of (b) temperature (5–40 °C) and (c) shear rate (0.1 to 1000 s^{-1}) at a fixed frequency of 1 Hz using a Kinexus Prime Ultra+ rheometer (NETZSCH Australia Pty Ltd, Sydney, Australia) with a compressed air flow of 4 bar. The measurements were taken with a gap height of 0.1504 mm using a cone-plate geometry (CP1/50 L2540 SS). (d) Extrusion printing of a GelMA droplet into a well of a 96-well culture plate, from a temperature-controlled printhead of a CELLINK BIO X6 bioprinter (CELLINK, Gothenburg, Sweden).

the storage modulus increased with higher GelMA concentration under both temperature conditions,[32] although 25 °C consistently yielded greater stiffness than 37 °C. More specifically, at 25 °C the storage modulus of 2.5%, 5.0%, 7.5% and 10% (w/v) GelMA were approximately 12.9 ± 2.6, 281.0 ± 71.5, 295.5 ± 26.4 and 1010.1 ± 13.2 Pa, respectively. At 37 °C, they were 15.9 ± 2.7, 146.6 ± 8.6, 193.3 ± 5.1 and 545.7 ± 25.2 Pa, respectively. GelMA hydrogels soften at elevated temperatures due to the thermosensitive properties of gelatin.[28] At lower temperatures, gelatin forms a physically crosslinked network via hydrogen bonding and chain entanglements, resulting in a firmer hydrogel.[33] As temperature increases, hydrogen bonds weaken, leading to a transition from a gel to a sol state and a reduction in the mechanical stiffness of the hydrogel.[33] This temperature-dependent behaviour is characteristic of gelatin-based hydrogels, including GelMA.[33]

The range of hydrogel stiffness measured aligns with the stiffness of the brain (100–400 Pa),[34-36] lung (800 Pa)[37] and breast (1000 Pa)[38] tissues, confirming its utility for tissue-mimicking and tumour-modelling applications. The 5% (w/v) GelMA was deemed optimal for GBM cell printing, with a stiffness of 146.6 ± 8.6 Pa, comparable to that of brain tissue. Moreover, Figure 3b reveals that the storage modulus (G') of GelMA hydrogel remains constant across the entire frequency sweep, measured at 37 °C with a constant strain of 0.1%. In contrast, the storage modulus decreased when strain exceeded 10%, regardless of the GelMA concentration (Figure 3c). Furthermore, the storage modulus was higher than the loss modulus

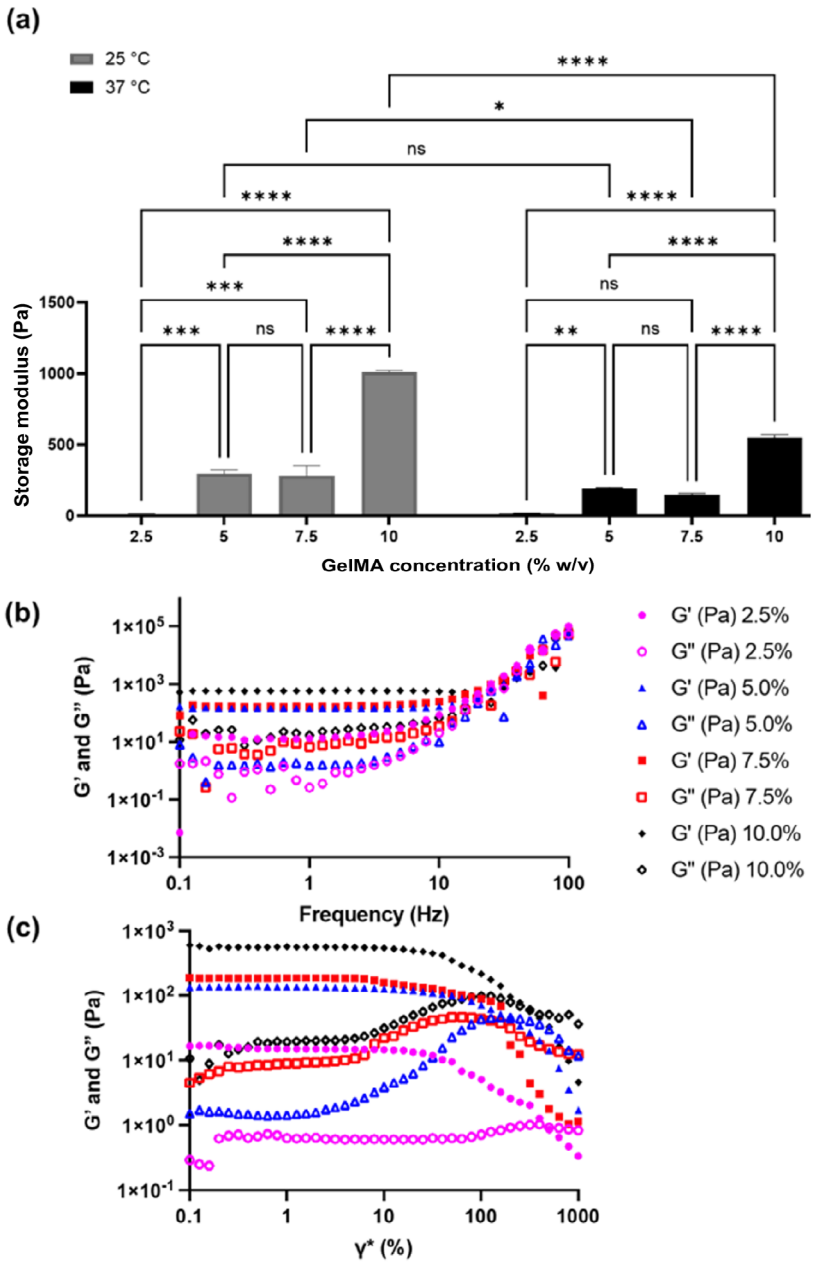


Figure 3. Rheology of pre-formed GelMA hydrogels at 2.5, 5.0, 7.5, and 10% (w/v). (a) Storage modulus of GelMA measured at 25 °C (grey bars) and 37 °C (black bars) after 30 min of incubation in DMEM medium. Representative shear moduli (G', filled symbols; G", open symbols) of GelMA hydrogels at 37 °C during (b) frequency and (c) strain amplitude sweep. Statistical analyses were performed using a two-way ANOVA ($F(3, 8) = 48.4$, $p < 0.001$) followed by Bonferroni post hoc test (*$p < 0.05$, **$p < 0.01$, ***$p < 0.001$, ****$p < 0.0001$).

at all GelMA concentrations, confirming hydrogel-like behaviour.

3.2. Generation of tumouroids and chemotherapy dose-response assay

Printed tumouroids were initially optimised with SF188 cells. The selected cell density (6×10^6 cells/mL in 5% GelMA solution) satisfied both the bioprinting and analytical requirements of the droplet model. This formulation provided sufficient viscosity for consistent droplet extrusion, maintained structural integrity following gelation, and preserved biological function. Furthermore,

the density supported droplet shape fidelity and the cell-cell interactions required for tumour tissue formation while minimising nozzle clogging and adverse effects on tumour cell viability. Importantly, it also ensured that cell viability measurements remained within the linear dynamic range of the PrestoBlue assay throughout drug exposure, thereby enabling accurate and quantitative evaluation of treatment responses.

Different printing pressures (16, 18 or 20 kPa) created relatively small (~6 µL), medium (~7 µL) and large droplets (~8 µL), respectively. A PrestoBlue assay performed on days 1, 2 and 5 confirmed increased metabolic activity over time for smaller and medium droplets, as shown in Figure S1. Although larger droplets showed higher metabolic activity on day 1, their activity did not increase thereafter. As such, further studies employed medium-sized constructs printed at 18 kPa, yielding a droplet volume of ~7 µL.

The responses of printed SF188 and KNS42 tumouroids to TMZ treatment were assessed by PrestoBlue assay (Figure 4a). Dose-response data showed a greater effect of TMZ on responder-cells of SF188 tumouroids compared to KNS42 tumouroids, with 50% inhibitory concentrations (IC_{50} values) of ~105.6 µM and ~135.5 µM, respectively (Figure 4b).[39,40] Furthermore, SF188 tumouroids comprised a smaller proportion of resistant cells compared to KNS42 tumouroids (~20% and ~70%, respectively), and normalised dose-response data for the responder-cell fraction yielded 50% effective concentrations (EC_{50} values) of 75.3 µM for SF188 and 144.4 µM for KNS42 tumoroids, corroborating the greater potency of TMZ on SF188 responder-cells. The larger TMZ IC_{50} observed for KNS42 tumouroids relative to SF188 tumouroids aligns with previously reported 2D monolayer data (SF188 ≈ 200 µM, KNS42 > 500 µM).[40] This concordance indicates that the 3D-bioprinted tumoroids preserved the intrinsic drug response hierarchy of the parental cell lines while providing a more physiologically relevant microenvironment.

3.3. MGMT expression

Given the established clinical relevance of MGMT in GBM, we examined the expression of the nuclear DNA repair

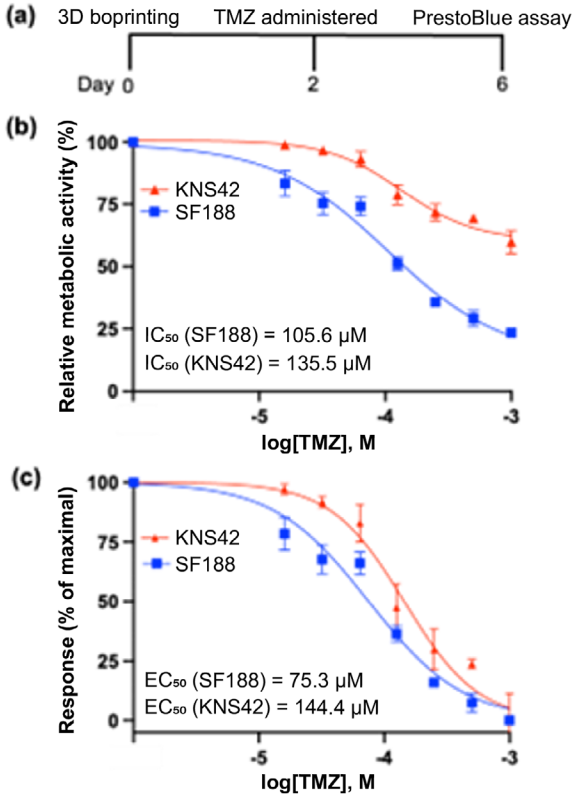


Figure 4. PrestoBlue metabolic activity assay of TMZ-treated 3D-printed SF188 and KNS42 tumouroids. (a) Schematic of the experimental setup. (b) TMZ dose-response curves depicting IC_{50} values and (c) normalised dose-response curves to calculate the EC_{50} values, after 4 days of treatment with 1000, 500, 250, 125, 62.5, 32, 16 and 0 µM TMZ.
Abbreviations: EC_{50}: 50% effective concentration; IC_{50}: 50% inhibitory concentration; TMZ: Temozolomide.

protein MGMT in bioprinted tumouroids. TMZ induces cytotoxicity through methylation of the O-6 position of guanine in DNA, and tumours harbouring *MGMT* promoter methylation typically exhibit reduced MGMT expression, impaired repair of O^6-methylguanine lesions, and increased sensitivity to TMZ. Conversely, elevated MGMT expression in tumours with an unmethylated-MGMT promoter confers resistance, attenuating TMZ-induced cytotoxicity.[41,42] While MGMT promoter methylation is the clinically established biomarker for predicting TMZ response, MGMT protein expression represents the functional endpoint of this pathway; accordingly, its assessment in bioprinted tumouroids provides a direct measure of DNA repair capacity and treatment response in a 3D tissue context, independent of upstream epigenetic regulation.

Immunohistochemistry indicated nuclear localisation of MGMT protein in cells from both untreated and TMZ-treated SF188 and KNS42 tumouroids (Figure 5a and 5b). Furthermore, quantitative analysis confirmed a dose-dependent increase in MGMT expression up to 64 μM TMZ, followed by a plateau for SF188 tumouroids (Figure 5c). In contrast, KNS42 tumouroids expressed lower overall MGMT levels, with no correlation with increasing TMZ dose (Figure 5c). This is consistent with the known methylation status of SF188 and KNS42 cells, typically characterised as MGMT-unmethylated and MGMT-methylated, respectively, and their corresponding resistance to TMZ (MGMT-dependent and -independent, respectively). Additionally, KNS42 cell resistance is linked to a PI3-kinase-mediated HOX/stem cell gene signature.[40] Other studies also indicate that the DNA repair mechanism in KNS42 cells operates through the base-excision repair (BER) pathway.[43,44] BER activity mediated by the enzyme 3-methylpurine-DNA glycosylase (MPG) efficiently repairs the N-methylated DNA adducts (such as N3-methyladenine) before the onset of cytotoxicity. Furthermore, RNA knockdown of MPG expression increases the sensitivity of KNS42 cells to TMZ, confirming its direct role in promoting resistance.[43] Together with inhibition of other key BER proteins, such as DNA polymerase beta (Pol-B), BER can also overcome TMZ resistance, making it a potentially critical therapeutic target in tumours with this specific resistance profile.[45,46] Additionally, a previous study using glioblastoma cell lines U87 and T98G with low and high MGMT expression, respectively, has shown that recurrence of GBM after TMZ treatment is driven by highly invasive drug-resistant cells.[47] Short-term (≤ 72 h) TMZ pulse transiently increases cell motility, a reversible EMT-like (glial mesenchymal transition, GMT) response, which occurs independently of MGMT. With prolonged TMZ exposure (30 days), only the MGMT expressing T98G cells survive, continue to proliferate, and permanently acquire a mesenchymal phenotype characterised by sustained up regulation of the EMT driver Snail 1 and the gap junction protein Cx43. These two factors reinforce each other in a positive feedback loop that drives persistent invasion and TMZ resistance. In contrast, MGMT deficient U87 cells accumulate lethal DNA damage, undergo apoptosis or senescence, and lose their invasive capacity, indicating that MGMT is not the initiator of EMT but rather provides a permissive repair background that allows the transient TMZ-induced EMT-like changes to evolve into a durable Snail 1/Cx43-driven invasive program.

3.4. MicroRNA expression analysis

KNS42 and SF188 tumouroids were cultured for 48 h, treated with various doses of TMZ (0, 64, 125, 250, 500, and 1000 μM) for 4 days, and subsequently dissociated for RNA extraction (Table S2). For all extracted samples, intact RNA was indicated by high RNA integrity number (RIN) scores (> 7.5), and electropherograms confirmed ribosomal RNA peaks at 28S and 18S, as well as small miRNAs (Figures S2 and S3). Analysis of miRNAs, including miR-490, miR-137, miR-876-3p, miR-876-5p, miR-448, miR-501-3p, and miR-191-5p (endogenous control) demonstrated that only miR-137 and miR-191-5p (endogenous control) were expressed in KNS42 cells, whilst SF188 cells expressed miR-876-3p, miR-876-5p, miR-137, and miR-191-5p (Figures S4–S17).

The copy number of the miRNAs expressed for each TMZ treatment condition was normalised to endogenous miR-191-5p expression, followed by further normalisation to the untreated (0 μM) TMZ group (Figure 6a–c). Figure 6a shows the relative expression of miR-137 for SF188 and KNS42 tumouroids treated with various doses of TMZ. For both tumouroids, a non-monotonic (biphasic) dose-effect is apparent, with miR-137 expression increasing up to 250 μM and 500 μM TMZ in SF188 and KNS42 tumouroids, respectively, followed by downregulation. Whilst the dose effects on miR-137 expression suggest comparable sensitivity of KNS42 and SF188 tumouroids up to 250 μM TMZ (*i.e.*, the point of peak miRNA expression for KNS42), further miRNA upregulation for SF188 tumouroids and successive downregulation for KNS42 tumouroids are consistent with previous reports of reduced miR-137 expression associated with TMZ resistance,[48-50] the aforementioned higher and lower sensitivity of SF188 and KNS42 tumouroids to TMZ, and reports of higher miR-137 expression associated with reduced cancer cell invasion, increased chemosensitivity,[51] inhibition of tumour growth[52] and induction of cellular senescence.[53] Although causality was not investigated in the current study, the association observed between miR-137 expression and TMZ sensitivity aligns with previous

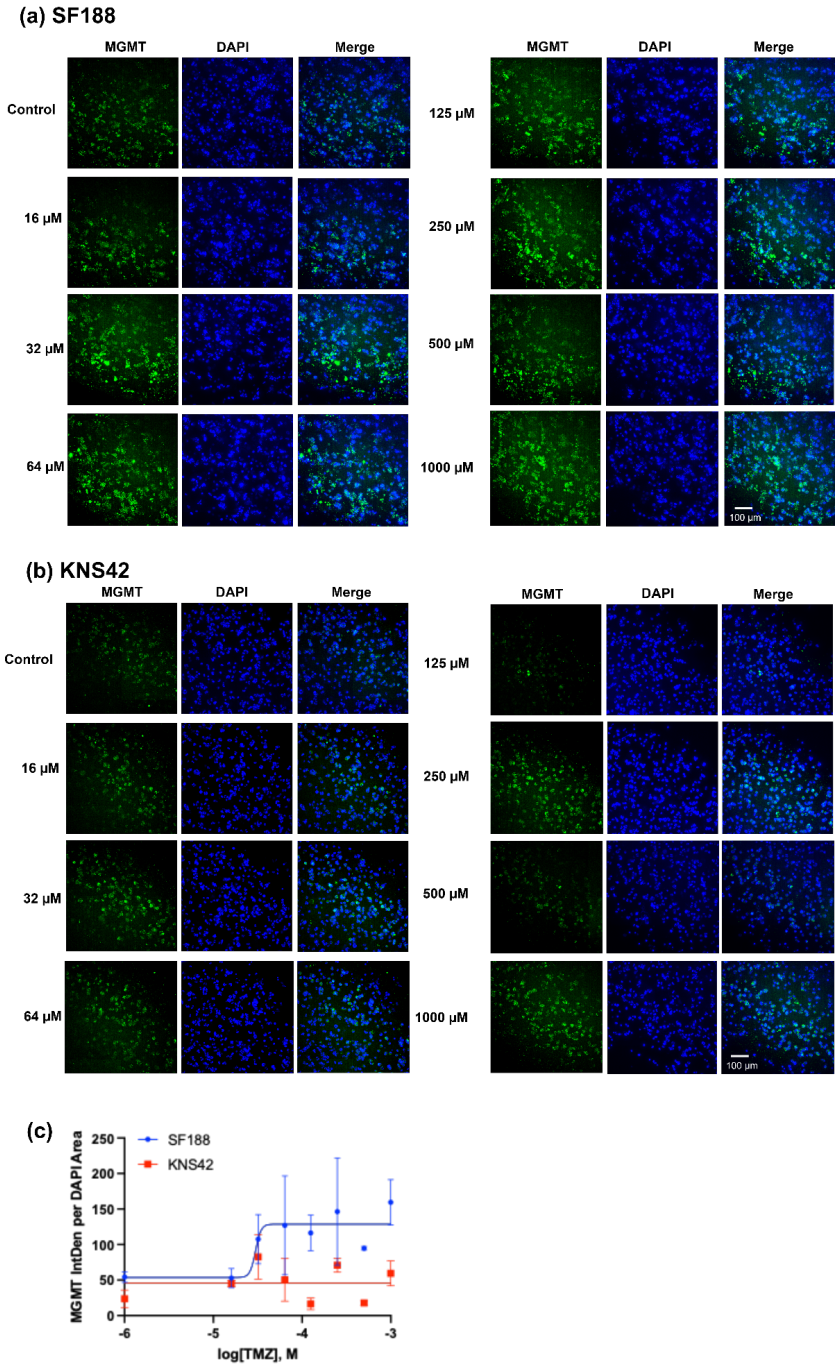


Figure 5. Immunohistochemistry-based assessment of MGMT expression in TMZ-treated 3D-printed SF188 and KNS42 tumouroids. Representative fluorescence microscopy images showing MGMT expression (green) localised to DAPI-stained (blue) nuclei in (a) SF188 and (b) KNS42 tumouroids after four days of TMZ treatment at doses ranging from 0 to 1000 μM. Scale bars = 100 μm. (c) Quantitative assessment of nuclear MGMT expression (integrated density; IntDen) normalised to DAPI-positive area in KNS42 (red bars) and SF188 (blue bars) tumouroids after TMZ treatment at doses ranging from 0 to 1000 μM and plotted using the four-parameter logistic (4PL) regression model for the line of best fit (estimated R^2 for SF188 = 0.409 and KNS42 = 0). Statistical analysis revealed a significant, dose-dependent increase in MGMT expression in SF188 tumouroids following TMZ treatment. This upregulation is statistically significant at higher concentrations compared to baseline ($p < 0.05$), suggesting an active adaptive response to DNA damage. In contrast, the KNS42 tumouroids showed no significant change in MGMT levels across all tested concentrations, indicating they lack the inducible MGMT expression of SF188 tumouroids. These data confirm that while cells of SF188 tumouroids upregulate DNA repair enzymes in response to chemical stress, KNS42 cells maintain a constant, low-level expression regardless of dose.
Abbreviations: MGMT: O^6-methylguanine-DNA methyltransferase; TMZ: Temozolomide.

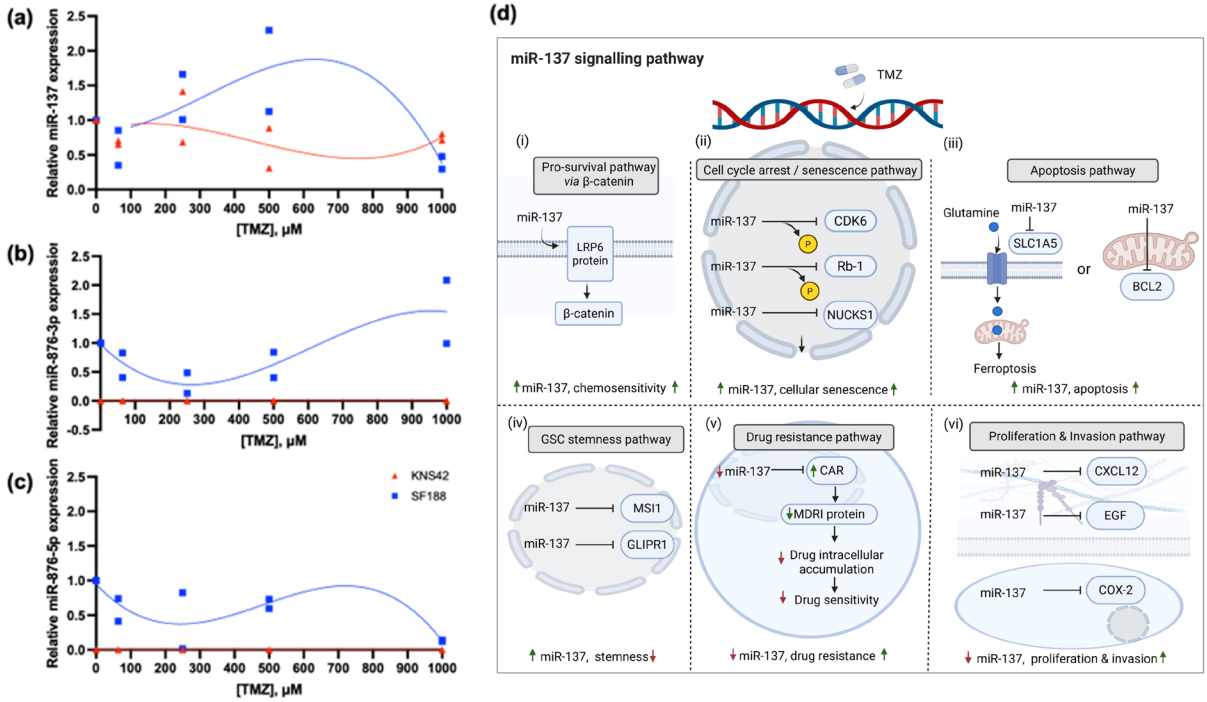


Figure 6. Relative expression levels of miRNAs from SF188 (blue squares) and KNS42 (red triangles) GBM tumouroids treated for 4 days with 0, 64, 125, 250, 500, and 1000 μM TMZ. (a) miR-137, (b) miR-876-3p, and (c) miR-876-5p. The miRNA expression for each TMZ condition was normalised to the level of expression for the untreated (0 μM) condition. Data was derived from two independent experiments ($n = 2$) and used for descriptive analysis. (d) Potential miR-137 signalling pathways for (i) pro-survival via ß-catenin, (ii) senescence, (iii) apoptosis, (iv) GSC stemness, (v) drug resistance and (vi) proliferation and invasion in response to TMZ treatment.
Abbreviations: GBM: Glioblastoma; GSC: Glioblastoma stem cell; TMZ: Temozolomide.

evidence demonstrating that miR-137 sensitises GBM cells to TMZ through targeting of LRP6. Furthermore, hypoxia-induced downregulation of miR-137 has been reported to drive TMZ resistance and tumour progression via activation of the LRP6/β-catenin signalling axis (Figure 6d(i)).[50,54] Moreover, miR-137 promotes cellular senescence by suppressing the phosphorylation of cyclin-dependent kinase 6 (CDK6), the retinoblastoma-associated protein-1 phosphorylation, and the expression of nuclear casein kinase and CDK substrate 1 (NUCKS1) protein, which are essential for cell division.[53] Additionally, miR-137 has been shown to induce glioma cell apoptosis either by directly targeting Bcl-2 or by regulating ferroptosis by targeting the glutamine transporter solute carrier family 1, member 5 (SLC1A5) in melanoma cancer cells (Figure 6d(iii)).[54,55] Furthermore, miR-137 suppresses glioma pathogenesis-related protein 1 (GLIPR1) and Musashi-1 (Msil-1), thereby reducing glioblastoma cell stemness (Figure 6d(iv)).[56] An increase in miR-137 correlates with decreased self-renewal capability. Previous studies also demonstrated that miR-137 negatively regulates the constitutive androstane receptor (CAR) and MDR1 (p-glycoprotein) by targeting Y-box binding protein-1 (YB-1) in breast cancer, leading to reduced intracellular doxorubicin levels and cellular sensitivity to doxorubicin (Figure 6d(v)).[57,58] Finally, miR-137 has been shown to directly target C-X-C motif ligand 12 (CXCL12), epidermal growth factor receptor (EGFR), and cyclooxygenase-2 (COX-2), and decreased miR-137 level is associated with increased proliferation and invasion (Figure 6d(vi)).[59-61]

Measurement of circulating miR-137 levels could serve as a non-invasive prognostic marker, with low miR-137 linked to decreased overall survival in patients.[62] While this biomarker offers valuable disease monitoring potential, our experimental model could also be used to test therapeutic interventions that restore or modulate miR-137 activity, thereby assessing whether correcting its dysregulation can improve outcomes. These findings, together with our own 3D tumour modelling data, support a role for miR-137 in the cellular response to TMZ treatment, particularly evident in SF188 tumouroids compared to KNS42 tumouroids.

Non-monotonic dose-effect relationships have previously been described for TMZ treatment of GBM cell line LN-229, where p-p53ser46 (pro-death) protein levels were initially upregulated for lower (12.5 μM and 25 μM) TMZ doses, subsequently plateauing for 50 μM and 75 μM TMZ treatments and then increasing again at higher doses (100 μM and 125 μM).[63] The latter effect is likely due to extensive DNA damage induced by higher TMZ doses, which triggers a rapid cell death pathway, such as apoptosis rather than senescence. It is important to note that this was observed only after 72 hours of TMZ exposure; no changes in expression occurred after just 24 hours of treatment, indicating sequential activation of pro-survival and pro-death factors in GBM cells exposed to TMZ across multiple cell cycles.[63] These time-dependent responses could have implications for the therapeutic use of TMZ, particularly highlighting the potential to modulate miRNA expression in different glioma subtypes.

Unlike miR-137, miR-876-3p and miR-876-5p were not expressed by KNS42 tumouroids (Figure 6b and 6c). miR-876-3p and miR-876-5p function as tumour suppressors.[64,65] The absence of these miRNAs is again consistent with the resistance of KNS42 tumouroids to TMZ treatment;[66] however, the aforementioned alternative mechanism of TMZ resistance of KNS42 cells may not rely on miR-876 modulation. In contrast, for SF188 tumouroids, a biphasic U-shaped dose-response relationship was observed for miR-876-3p, with miR-876-5p expression decreasing towards negligible levels at 1000 μM TMZ. Furthermore, the interaction between miRNAs and other regulatory molecules, such as circRNAs, adds an extra layer of complexity, as these interactions can sequester miRNAs and prevent them from performing their tumour-suppressive roles. Therefore, understanding how miRNAs contribute to tumour resistance could reveal new therapeutic targets and strategies to overcome resistance in glioblastoma and other cancers. Examining these relationships can provide insights into how targeting these miRNAs or their regulatory networks might improve treatment outcomes. Our findings align with a previous study that identified circ_0043949 as a sponge for miR-876-3p. Inhibition of miR-876-3p countered the role of circ_0043949 in TMZ resistance, through the miR-876-3p/ITGA1 pathway.[66]

4. Conclusion

In conclusion, this study highlights the development and application of a high-throughput 3D-bioprinted human brain tumour model using GelMA-based bioink to investigate GBM biology and drug response. By first optimising the rheological properties of the GelMA hydrogel, we aimed to mimic the physicochemical properties of human brain tissue to support GBM cells, including those in the tumour microenvironment, for cell survival, growth, and chemotherapeutic treatment. By precisely controlling and measuring the rheological parameters (viscosity, yield stress, viscoelastic moduli), we optimised print fidelity, shape retention, and cellular viability during and after tumour bioprinting. GelMA flow was defined and controlled under printing stress, followed by solidification to form reproducibly stable, 3D GBM tumour constructs with biological functionality. The models were also used to assess responses to chemotherapy, providing insights into the molecular mechanisms underlying GBM chemosensitivity and resistance. In addition to profiling metabolic activity for drug dose response, we employed advanced ddPCR miRNA profiling to identify differential mechanisms of drug action between GBM cell lines, affirming the model's potential for personalised drug screening and therapeutic interventions. Furthermore, this platform demonstrates the potential for studying 3D-printed tumouroids generated from patient-derived primary cells, such as cells obtained from tissue fragments collected using a Cavitronic Ultrasonic Surgical Aspirator (CUSA) device. CUSA-derived constructs could contain GBM cells, glioma stem cells, astrocytes, vascular cells, immune cells, neurons, and hypoxia gradients, capturing tumour-stroma interactions influencing disease progression and drug response. Furthermore, validation of cellular senescence will complement current observations with a comprehensive molecular and functional marker panel, including p16INK4a and p21 expression, γH2AX foci accumulation, IL-6/IL-8 secretion, and SA-β-galactosidase activity. Primary cell profiling could extend to extracellular vesicle (EV)-associated miRNAs released from bioprinted constructs, as a promising "next-generation" strategy for biomarker discovery and preclinical modelling. Although our tumouroids represent a relatively simple model within the broader tumouroid landscape, our findings demonstrate their utility as a scalable and accessible platform for *in vitro* tumour modelling and the preclinical evaluation of emerging therapeutic strategies for GBM. By coupling advanced 3D bioprinting technologies with miRNA analytics, the models have the potential to establish a new paradigm for biomarker discovery, drug screening, and precision oncology.

Acknowledgments

We acknowledge the Arto Hardy Family, SurFebruary Cancer Research Fund, Tour de Cure, Tregaskis Foundation, the Yip family, Ian Potter Foundation and NSW Office for Health and Medical Research for financial support. Graphics were created using BioRender.com.

Funding

This work was funded by Arto Hardy Family, SurFebruary Cancer Research Fund, Tour de Cure, Tregaskis Foundation, Yip family, Ian Potter Foundation and NSW Office for Health and Medical Research.

Conflict of interest

Jeremy Crook is an Editorial Board Member of this journal, but was not in any way involved in the editorial and peer-review process conducted for this paper, directly or indirectly. The authors declare they have no competing interests.

Author contributions

Conceptualization: Eva Tomaskovic-Crook, Kimberley L. Alexander, Jeremy Micah Crook
Data curation: Panthipa Suwannakot, Eva Tomaskovic-Crook
Formal analysis: Panthipa Suwannakot, Eva Tomaskovic-Crook, Jeremy Micah Crook
Funding acquisition: Eva Tomaskovic-Crook, Kimberley L. Alexander, Jeremy Micah Crook
Investigation: Panthipa Suwannakot, Eva Tomaskovic-Crook
Methodology: Panthipa Suwannakot, Eva Tomaskovic-Crook, Jeremy Micah Crook
Project administration: Eva Tomaskovic-Crook, Jeremy Micah Crook
Resources: Eva Tomaskovic-Crook, Jeremy Micah Crook
Supervision: Eva Tomaskovic-Crook, Jeremy Micah Crook
Validation: Panthipa Suwannakot
Visualization: Panthipa Suwannakot, Eva Tomaskovic-Crook, Jeremy Micah Crook
Writing–original draft: Panthipa Suwannakot Eva Tomaskovic-Crook, Jeremy Micah Crook
Writing–review & editing: All authors

Ethics approval and consent to participate

Not applicable.

Consent for publication

Not applicable.

Availability of data

The data that support the findings of this study are available from the corresponding authors upon reasonable request.

References

1. Ostrom QT, Cioffi G, Gittleman H, *et al*. CBTRUS statistical report: primary brain and other central nervous system tumors diagnosed in the United States in 2012–2016. *Neuro-oncology*. 2019;21(Supplement_5):v1-v100.

   doi: 10.1093/neuonc/noz150

2. Llaguno SA, Chen J, Kwon C-H, *et al*. Malignant astrocytomas originate from neural stem/progenitor cells in a somatic tumor suppressor mouse model. *Cancer cell*. 2009;15(3):240.

   doi: 1016/j.ccr.2009.02.008

3. Lee JH, Lee JE, Kahng JY, *et al*. Human glioblastoma arises from subventricular zone cells with low-level driver mutations. *Nature*. 2018;560(7717):243-247.

   doi: 10.1038/s41586-018-0389-3

4. Gilbert MR, Dignam JJ, Armstrong TS, *et al*. A randomized trial of bevacizumab for newly diagnosed glioblastoma. *N Engl J Med*. 2014;370(8):699-708.

   doi: 10.1056/NEJMoa1308573

5. Stupp R, Taillibert S, Kanner A, *et al*. Effect of tumor-treating fields plus maintenance temozolomide vs maintenance temozolomide alone on survival in patients with glioblastoma: a randomized clinical trial. *J Am Med Assoc*. 2017;318(23):2306-2316.

   doi: 10.1001/jama.2017.18718

6. Zanders ED, Svensson F, Bailey DS. Therapy for glioblastoma: is it working? *Drug Discov Today*. 2019;24(5):1193-1201.

   doi: 10.1016/j.drudis.2019.03.008

7. Foglizzo V, Cocco E, Marchiò S. Advanced cellular models for preclinical drug testing: from 2D cultures to organ-on-a-chip technology. *Cancers*. 2022;14(15):3692.

   doi: 10.3390/cancers14153692

8. Jensen C, Teng Y. Is it time to start transitioning from 2D to 3D cell culture? *Front Mol Biosci*. 2020;7:33.

   doi: 10.3389/fmolb.2020.00033

9. Nii M, Lai JH, Keeney M, *et al*. The effects of interactive mechanical and biochemical niche signaling on osteogenic differentiation of adipose-derived stem cells using combinatorial hydrogels. *Acta Biomater*. 2013;9(3):5475-5483.

   doi: 10.1016/j.actbio.2012.11.002

10. DeForest CA, Sims EA, Anseth KS. Peptide-functionalized click hydrogels with independently tunable mechanics and chemical functionality for 3D cell culture. *Chem Mater*. 2010;22(16):4783-4790.

    doi: 10.1021/cm101391y

11. Tomaskovic-Crook E, Crook JM. Clinically amendable, defined, and rapid induction of human brain organoids from induced pluripotent stem cells. In: *Methods in Molecular Biology*. New York, NY: Springer New York; 2017:13-22.

    doi: 10.1007/7651_2017_95

12. Tomaskovic-Crook E, Higginbottom SL, Zhang B, Bourke J, Wallace GG, Crook JM. Defined, simplified, scalable, and clinically compatible hydrogel-based production of human brain organoids. *Organoids*. 2023;2(1):20-36.

doi: 10.3390/organoids2010002

13. Tang M, Xie Q, Gimple RC, *et al*. Three-dimensional bioprinted glioblastoma microenvironments model cellular dependencies and immune interactions. *Cell research*. 2020;30(10):833-853.

doi: 10.1038/s41422-020-0338-1

14. Giunti L, Da Ros M, De Gregorio V, *et al*. A microRNA profile of pediatric glioblastoma: The role of NUCKS1 upregulation. *Mol Clin Oncol*. 2019;10(3):331-338.

doi: 10.3892/mco.2019.1795

15. Gaur A, Jewell DA, Liang Y, *et al*. Characterization of microRNA expression levels and their biological correlates in human cancer cell lines. *Cancer Res*. 2007;67(6):2456-2468.

doi: 10.1158/0008-5472.CAN-06-2698

16. Godlewski J, Nowicki MO, Bronisz A, *et al*. Targeting of the Bmi-1 oncogene/stem cell renewal factor by microRNA-128 inhibits glioma proliferation and self-renewal. *Cancer Res*. 2008;68(22):9125-9130.

doi: 10.1158/0008-5472.CAN-08-2629

17. Kim H, Huang W, Jiang X, Pennicooke B, Park PJ, Johnson MD. Integrative genome analysis reveals an oncomir/oncogene cluster regulating glioblastoma survivorship. *Proc Natl Acad Sci USA*. 2010;107(5):2183-2188.

doi: 10.1073/pnas.0909896107

18. Cui Q, Yu Z, Purisima EO, Wang E. Principles of microRNA regulation of a human cellular signaling network. *Mol Syst Biol*. 2006;2(1):46.

doi: 10.1038/msb4100089

19. Bartel DP. MicroRNAs: genomics, biogenesis, mechanism, and function. *Cell*. 2004;116(2):281-297.

doi: 10.1016/S0092-8674(04)00045-5

20. Piwecka M, Rolle K, Belter A, *et al*. Comprehensive analysis of microRNA expression profile in malignant glioma tissues. *Mol Oncol*. 2015;9(7):1324-1340.

doi: 10.1016/j.molonc.2015.03.007

21. Wang M, Xie H, Stellpflug W, *et al*. BTECH: a platform to integrate genomic, transcriptomic and epigenomic alterations in brain tumors. *Neuroinformatics*. 2011;9:59-67.

doi: 10.1007/s12021-010-9091-9

22. Belter A, Rolle K, Piwecka M, Fedoruk-Wyszomirska A, Naskręt-Barciszewska MZ, Barciszewski J. Inhibition of miR-21 in glioma cells using catalytic nucleic acids. *Sci Rep*. 2016;6(1):24516.

doi: 10.1038/srep24516

23. Zhang S, Han L, Wei J, *et al*. Combination treatment with doxorubicin and microRNA-21 inhibitor synergistically augments anticancer activity through upregulation of tumor suppressing genes. *Int J Oncol*. 2015;46(4):1589-1600.

doi: 10.3892/ijo.2015.2841

24. Palizkaran Yazdi M, Barjasteh A, Moghbeli M. MicroRNAs as the pivotal regulators of Temozolomide resistance in glioblastoma. *Mol Brain*. 2024;17(1):42.

doi: 10.1186/s13041-024-01113-6

25. Tolue Ghasaban F, Maharati A, Zangouei AS, Zangooie A, Moghbeli M. MicroRNAs as the pivotal regulators of cisplatin resistance in head and neck cancers. *Cancer Cell Int*. 2023;23(1):170.

doi: 10.1186/s12935-023-03010-9

26. Schindelin J, Arganda-Carreras I, Frise E, *et al*. Fiji: an open-source platform for biological-image analysis. *Nat methods*. 2012;9(7):676-682.

doi: 10.1038/nmeth.2019

27. Tomaskovic-Crook E, Zhang P, Ahtiainen A, *et al*. Human neural tissues from neural stem cells using conductive biogel and printed polymer microelectrode arrays for 3D electrical stimulation. *Adv Healthc Mater*. 2019;8(15):1900425.

doi: 10.1002/adhm.201970062

28. James EC, Tomaskovic-Crook E, Crook JM. Engineering 3D Scaffold-Free Nanoparticle-Laden Stem Cell Constructs for Piezoelectric Enhancement of Human Neural Tissue Formation and Function. *Adv Sci*. 2024;11(40):2310010.

doi: 10.1002/advs.202470239

29. Sun M, Sun X, Wang Z, Guo S, Yu G, Yang H. Synthesis and properties of gelatin methacryloyl (GelMA) hydrogels and their recent applications in load-bearing tissue. *Polymers*. 2018;10(11):1290.

doi: 10.3390/polym10111290

30. Liu W, Heinrich MA, Zhou Y, *et al*. Extrusion bioprinting of shear-thinning gelatin methacryloyl bioinks. *Adv Healthc Mater*. 2017;6(12):1601451.

doi: 10.1002/adhm.201770062

31. Padilla C, Quero F, Pępczyńska M, *et al*. Understanding the molecular conformation and viscoelasticity of low sol-gel transition temperature gelatin methacryloyl suspensions. *Int J Mol Sci*. 2023;24(8):7489.

doi: 10.3390/ijms24087489

32. Yu K, Zhang X, Sun Y, *et al*. Printability during projection-based 3D bioprinting. *Bioact Mater*. 2022;11:254-267.

doi: 10.1016/j.bioactmat.2021.09.021

33. Park HE, Gasek N, Hwang J, Weiss DJ, Lee PC. Effect of temperature on gelation and cross-linking of gelatin methacryloyl for biomedical applications. *Phys Fluids*. 2020;32(3).

doi: 10.1063/1.5144896

34. Budday S, Nay R, de Rooij R, *et al*. Mechanical properties of gray and white matter brain tissue by indentation. *J Mech Behav Biomed Mater*. 2015;46:318-330.

doi: 10.1016/j.jmbbm.2015.02.024

35. Kaster T, Sack I, Samani A. Measurement of the hyperelastic properties of ex vivo brain tissue slices. *J Biomech*. 2011;44(6):1158-1163.

doi: 10.1016/j.jbiomech.2011.01.019

36. Jagielska A, Norman AL, Whyte G, Vliet KJV, Guck J, Franklin RJ. Mechanical environment modulates biological properties of oligodendrocyte progenitor cells. *Stem Cells Dev*. 2012;21(16):2905-2914.

doi: 10.1089/scd.2012.0189

37. Polio SR, Kundu AN, Dougan CE, *et al*. Cross-platform mechanical characterization of lung tissue. *PloS ONE*. 2018;13(10):e0204765.

doi: 10.1371/journal.pone.0204765

38. Levental KR, Yu H, Kass L, *et al*. Matrix crosslinking forces tumor progression by enhancing integrin signaling. *Cell*. 2009;139(5):891-906.

doi: 10.1016/j.cell.2009.10.027

39. Pötschke R, Gielen G, Pietsch T, *et al*. Musashi1 enhances chemotherapy resistance of pediatric glioblastoma cells in vitro. *Pediatr Res*. 2020;87(4):669-676.

doi: 10.1038/s41390-019-0628-9

40. Gaspar N, Marshall L, Perryman L, *et al*. MGMT-independent temozolomide resistance in pediatric glioblastoma cells associated with a PI3-kinase–mediated HOX/stem cell gene signature. *Cancer Res*. 2010;70(22):9243-9252.

doi: 10.1158/0008-5472.CAN-10-1250

41. Weller M, Stupp R, Reifenberger G, *et al*. MGMT promoter methylation in malignant gliomas: ready for personalized medicine? *Nat Rev Neurol*. 2010;6(1):39-51.

doi: 10.1038/nrneurol.2009.197

42. Kaina B, Christmann M, Naumann S, Roos WP. MGMT: key node in the battle against genotoxicity, carcinogenicity and apoptosis induced by alkylating agents. *DNA repair*. 2007;6(8):1079-1099.

doi: 10.1016/j.dnarep.2007.03.008

43. Agnihotri S, Burrell K, Buczkowicz P, *et al*. ATM regulates 3-methylpurine-DNA glycosylase and promotes therapeutic resistance to alkylating agents. *Cancer Discov*. 2014;4(10):1198-1213.

doi: 10.1158/2159-8290.CD-14-0157

44. Mathews LA, Cabarcas SM, Farrar WL. DNA repair: the culprit for tumor-initiating cell survival? *Cancer Metastasis Rev*. 2011;30:185-197.

doi: 10.1007/s10555-011-9277-0

45. Trivedi RN, Almeida KH, Fornsaglio JL, Schamus S, Sobol RW. The role of base excision repair in the sensitivity and resistance to temozolomide-mediated cell death. *Cancer Res*. 2005;65(14):6394-6400.

doi: 10.1158/0008-5472.CAN-05-0715

46. Pu J, Yuan K, Tao J, *et al*. Glioblastoma multiforme: an updated overview of temozolomide resistance mechanisms and strategies to overcome resistance. *Discover Oncol*. 2025;16(1):731.

doi: 10.1007/s12672-025-02567-3

47. Kochanowski P, Catapano J, Pudełek M, *et al*. Temozolomide induces the acquisition of invasive phenotype by o6-methylguanine-dna methyltransferase (Mgmt)+ glioblastoma cells in a snail-1/cx43-dependent manner. *Int J Mol Sci*. 2021;22(8):4150.

doi: 10.3390/ijms22084150

48. Chen M, Cheng Y, Yuan Z, Wang F, Yang L, Zhao H. NCK1-AS1 increases drug resistance of glioma cells to temozolomide by modulating miR-137/TRIM24. *Cancer Biother Radiopharm*. 2020;35(2):101-108.

doi: 10.1089/cbr.2019.3054

49. Lu Y, Guo G, Hong R, *et al*. LncRNA HAS2-AS1 promotes glioblastoma proliferation by sponging miR-137. *Front Oncol*. 2021;11:634893.

doi: 10.3389/fonc.2021.634893

50. Li D-M, Chen Q-D, Wei G-N, *et al*. Hypoxia-induced miR-137 inhibition increased glioblastoma multiforme growth and chemoresistance through LRP6. *Front Oncol*. 2021;10:611699.

doi: 10.3389/fonc.2020.611699

51. Tunca B, Tezcan G, Cecener G, *et al*. Olea europaea leaf extract alters microRNA expression in human glioblastoma cells. *J Cancer Res Clin Oncol*. 2012;138(11):1831-1844.

doi: 10.1007/s00432-012-1261-8

52. Xiao J, Peng F, Yu C, *et al*. microRNA-137 modulates pancreatic cancer cells tumor growth, invasion and sensitivity to chemotherapy. *Int J Clin Exp Pathol*. 2014;7(11):7442-7450.

53. Wang Y, Chen R, Zhou X, *et al*. miR-137: a novel therapeutic target for human glioma. *Mol Ther-Nucl Acids*. 2020;21:614-622.

doi: 10.1016/j.omtn.2020.06.028

54. Luo M, Wu L, Zhang K, *et al*. miR-137 regulates ferroptosis

by targeting glutamine transporter SLC1A5 in melanoma. *Cell Death Differ*. 2018;25(8):1457-72.

55. Sun G, Cao Y, Shi L, *et al*. Overexpressed miRNA-137 inhibits human glioma cells growth by targeting Rac1. *Cancer Biother Radiopharm*. 2013;28(4):327-334.

doi: 10.1089/cbr.2012.1380

56. Velasco MX, Kosti A, Guardia GD, *et al*. Antagonism between the RNA-binding protein Musashi1 and miR-137 and its potential impact on neurogenesis and glioblastoma development. *Rna*. 2019;25(7):768-782.

doi: 10.1261/rna.069211.118

57. Zhu X, Li Y, Shen H, *et al*. miR-137 restoration sensitizes multidrug-resistant MCF-7/ADM cells to anticancer agents by targeting YB-1. *Acta Biochim Biophys Sin*. 2013;45(2):80-86.

doi: 10.1093/abbs/gms099

58. Takwi AA, Wang Y-M, Wu J, Michaelis M, Cinatl J, Chen T. miR-137 regulates the constitutive androstane receptor and modulates doxorubicin sensitivity in parental and doxorubicin-resistant neuroblastoma cells. *Oncogene*. 2014;33(28):3717-3729.

doi: 10.1038/onc.2013.330

59. Chen L, Wang X, Wang H, *et al*. miR-137 is frequently down-regulated in glioblastoma and is a negative regulator of Cox-2. *Eur J Cancer*. 2012;48(16):3104-3111.

doi: 10.1016/j.ejca.2012.02.007

60. Li D, Shan W, Fang Y, Wang P, Li J. miR-137 acts as a tumor suppressor via inhibiting CXCL12 in human glioblastoma. *Oncotarget*. 2017;8(60):101262.

doi: 10.18632/oncotarget.20589

61. Zhang Z, Song X, Tian H, *et al*. MicroRNA-137 inhibits growth of glioblastoma through EGFR suppression. *Am J Transl Res*. 2017;9(3):1492-1499.

62. Woo PY, Li Y, Chan AH, *et al*. A multifaceted review of temozolomide resistance mechanisms in glioblastoma beyond O-6-methylguanine-DNA methyltransferase. *Glioma*. 2019;2(2):68-82.

doi: 10.4103/glioma.glioma_3_19

63. He Y, Kaina B. Are there thresholds in glioblastoma cell death responses triggered by temozolomide? *Int J Mol Sci*. 2019;20(7):1562.

doi: 10.3390/ijms20071562

64. Yang F, Zhao WJ, Jia CL, Li XK, Wang Q, Chen ZL. MicroRNA-876-3p functions as a tumor suppressor gene and correlates with cell metastasis in pancreatic adenocarcinoma via targeting JAG2. *Am J Cancer Res*. 2018;8(4):636-649.

65. Ma B, Xu J, Chen G, *et al*. miR-876-5p exerts tumor suppressor function by targeting TWIST1 and regulating the epithelial-mesenchymal transition in glioblastoma. *Int J Clin Exp Med*. 2020;13:1454-1463.

66. Li X, Wang N, Leng H, Yuan H, Xu L. Hsa_circ_0043949 reinforces temozolomide resistance via upregulating oncogene ITGA1 axis in glioblastoma. *Metab Brain Dis*. 2022;37(8):2979-2993.

doi: 10.1007/s11011-022-01069-3